Study of Resonance Issues between DFIG-based Offshore Wind Farm and HVDC Transmission

Yonggang Zhang, Christian Klabunde, Martin Wolter
Institute of Electric Power Systems
Otto von Guericke University Magdeburg
Magdeburg, Germany
yonggang.zhang@ovgu.de

***Abstract*—Wide-frequency range of resonances can occur in HVDC-connected DFIG-based offshore wind farm (OWF), thus induce large harmonic distortion or endanger system stability. Previous studies usually treat OWF as a single-machine system without considering the switching states of individual wind turbines and collecting cables, or ignore the converter responses to wind speed variation and generation control order. In this paper, such factors are included in the modelling of OWF. Their impacts on resonance frequency, amplification level and the occurrence of negative damping are analyzed applying the resonance mode analysis method. Harmonic stability and power quality issues are demonstrated for the frequency range from several Hz to a few kHz. Simulations in MATLAB/Simulink validate the analytical results. Additionally, resonance damping strategies are discussed regarding the identified resonances in widely spread frequencies.**

***Index Terms*—DFIG, HVDC, harmonic stability, power quality, resonance mode analysis (RMA).**

I. Introduction

Resonance issues in converter-interfaced power systems have attracted intentions in industry and academia for years. For the application of HVDC connected OWF employing DFIG-based wind turbines (WTs), the interaction among converter-interfaced grid components and with other passive grid components may introduce wide frequency range of resonances. The stimulation of such resonances may cause the violation of harmonic distortion limits as stipulated in IEEE Std 519-2014 [1] or incur instability when under poor or negative damping conditions. Possible consequences are the tripping of turbines, blocking of HVDC converter, or physical damages of sensitive grid components. Field experiences on such issues are reported in [2]-[4].

When connected with HVDC transmission, DFIG-based WTs are prone to sub-synchronous resonance (SSR) due to the inductive and capacitive (LC) interaction at SSR frequencies [5]. Damping of the SSR is typically low or negative due to the negative resistance induced by the negative slip ratio of the induction generator and converter controls [6]. For large-scale OWFs, the widely distributed WT collecting cables have large cumulative capacitive effect, thus strongly participate in the resonances at hundreds or thousands of Hz [7]. Noted that the risk of above resonances is susceptible to the variation of grid topology and operating conditions [8], [9].

In recent years, impedance based methods have been intensively applied in resonance analysis. Accurate impedance model of DFIG incorporating double-loop PI control dynamics, mirror frequency coupling and DC side dynamics is built in [10], but the model has complicated analytical representation. It has been proved that neglecting outer control loop and DC side dynamics is acceptable for resonance studies down to a few Hz [11]. Zong et al [12] try to build an accurate impedance model for wind farm by considering a unified dq-frame for all WTs, but the involved phase difference between global and local reference frames varies with operating conditions and needs to be identified each time when operating point changes, thus make impedance methods lose the advantage in convenience. Chen et al [13] compare existing aggregation methods of wind farm and demonstrates that neglecting the coupling between positive and negative sequence impedances may not be effective for quantitative stability analysis, but it is useful for identifying the resonance points of wind farm and analyzing their risk qualitatively. From the above, it is feasible for this work to simplify the impedance modelling of DFIG-based WT and OWF while maintaining their accuracy for resonance analysis.

Generally, Nyquist and Bode-plot methods are applied to study resonances at the point of common coupling (PCC), which requires equalizing a system into load and source subsystems [14], [15]. Since the severest harmonic distortion can occur at any bus of a system, simply investigating the PCC condition is obviously not in favor of identifying resonance source and developing mitigation strategies [16]. Therefore, this work adopts an impedance network method, i.e. resonance mode analysis (RMA), to address the resonance issues related to wind speed variation and grid topology change. The locations where resonances can be most easily excited are identified through bus participation factor analysis [17]. Additionally, traditional impedance-based RMA only evaluates the amplitude of modal impedance, this work also uses the damping information embedded in phase angle or the real part of modal impedance in assessing stability.

Y. Zhang thanks for the financial support from *China Scholarship Council (CSC File No.201608320229).*

The rest of this paper is organized as follows: Section II introduces the investigated system and its small-signal impedance modelling. Section III presents the impact of OWF operating conditions on the risk of resonances and a discussion on damping strategies. Section IV concludes the work.

II. System Description and Impedance Modelling

This paper investigates the resonances of an offshore grid composed by a 400 MW DFIG-based OWF and a ±150 kV HVDC connection. Typical German offshore grid configuration is adopted, as shown in Fig. 1 [2], [3]. On the left side are two 33 kV collector systems, each gathering 40 WTs through 6 wind arrays, in which there are 2 arrays, each consisting of 4 WTs, and there are 4 arrays, each consisting of 8 WTs. In the middle are two OWF platforms, which are connected to the right-side HVDC platform through short 155 kV AC cables. This offshore system is connected to main onshore grid through the HVDC link. Setup of collector cables is given in Fig. 1. Cable data is estimated from ABB user's guide for submarine cable systems [18], as presented in Table I.

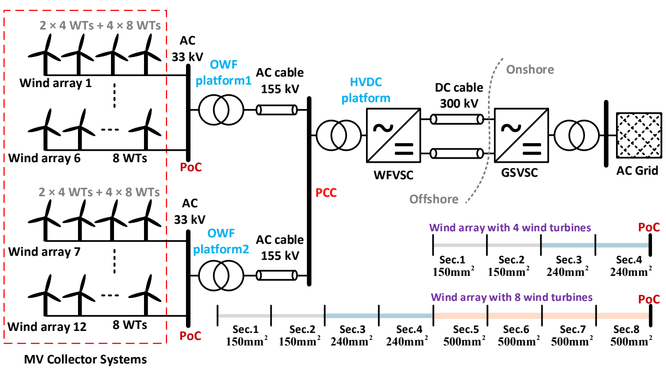

Fig. 1 Structure of the investigated system

Cable Type	Cross section	Length	Electrical Parameters per km
1	150 mm^2	1 km	$R = 0.16\,\Omega, L = 0.41\text{ mH}, C = 0.21\,\mu\text{F}$
2	240 mm^2	1 km	$R = 0.098\,\Omega, L = 0.38\text{ mH}, C = 0.24\,\mu\text{F}$
3	500 mm^2	1 km	$R = 0.05\,\Omega, L = 0.34\text{ mH}, C = 0.32\,\mu\text{F}$

TABLE I. Parameters of Collector Cables

Since the series impedance of each cable section is small, it is reasonable to assume that in-service wind turbines operate under same conditions, i.e. with same terminal voltage and current injection. Then to relieve computational burden, each medium-voltage (MV) collector cable system is equalized into a single cable applying the equivalent power-loss method [5], [19]. Series impedance and shunt admittance of the adopted pi model are represented by (1) and (2), where $R_{m,n}$, $L_{m,n}$ and $C_{m,n}$ denote the parameters of the n^{th} cable section in array m, M denotes the total amount of arrays, and N_m denotes the amount of WTs in array m. Parameters of the aggregated WT are linearly related to power rating, which can be easily obtained by dividing/multiplying wind turbine number, as given in Table II. When the number of operating WTs varies or grid topology changes, the aggregated models can be adjusted accordingly.

$$Z_{\text{mv}}(s) = \sum_{m=1}^{M}\sum_{n=1}^{N_m} n^2 \left(R_{m,n} + sL_{m,n}\right) \Big/ \left(\sum_{m=1}^{M} N_m\right)^2 \tag{1}$$

$$Y_{\text{mv}}(s) = \sum_{m=1}^{M}\sum_{n=1}^{N_m} sC_{m,n} \tag{2}$$

Aggregated WTs	N_{wt} (quantity)
Rated Voltage / Power	950 V / 5 MW $\cdot N_{\text{wt}}$
DFIG generator (pu)	$R_s = 0.023, L_{\sigma s} = 0.18, R_r = 0.016, L_{\sigma r} = 0.16, L_m = 2.9$
GSC side reactor (pu)	$R_p = 0.003,\ L_p = 0.3$
Current controllers	GSC: $K_{gp} = 0.83,\ K_{gi} = 5$, RSC: $K_{rp} = 0.15,\ K_{ri} = 2$
Terminal filter	600 kvar $\cdot N_{\text{wt}}$, Q=50 (quality factor)
Step-up transformer	5.5 MVA $\cdot N_{\text{wt}}$, 0.95 /33 kV, $u_k = 5\%$, $u_r = 0.17\%$
Sampling period	$T_s = 5\ \mu s$
Switching frequency	1600 Hz
PLL	$K_{pp} = 16,\ K_{pi} = 50$

TABLE II. Parameters of Single or Aggregated DFIG-based WT

Aggregated representation of the investigated system is shown in Fig. 2, in which grid parameters and the control blocks of DFIG converters and HVDC converter are included. For DFIG-based wind turbine, there are two back-to-back converters and an induction machine. Grid side converter (GSC) controls DC side voltage, while rotor side converter (RSC) controls rotor speed and reactive power.

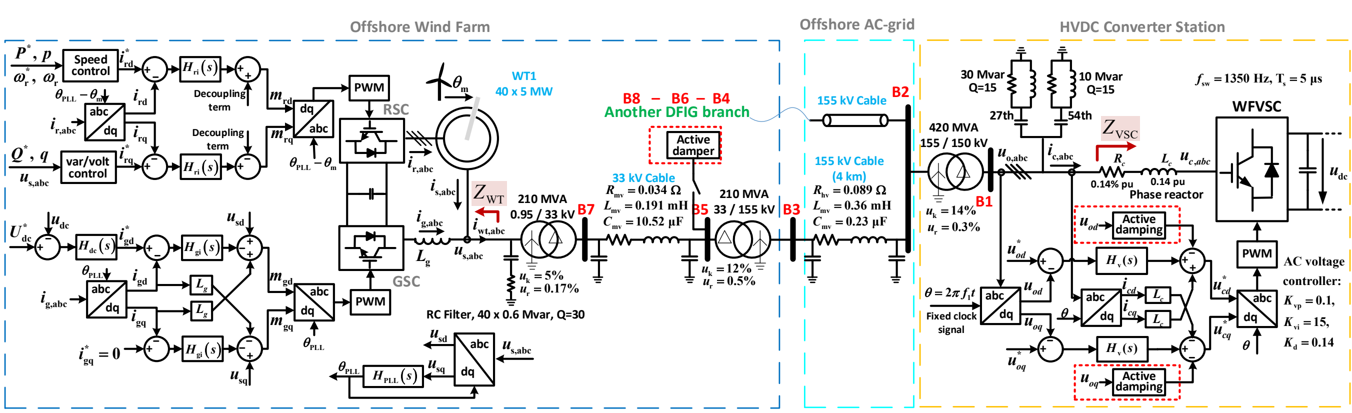

Fig. 2 Aggregated representation of the investigated HVDC connected DFIG-based OWF

$$Z_{\mathrm{gp}}(s)=\frac{R_{\mathrm{g}}+L_{\mathrm{g}}s-\left[H_{\mathrm{gi}}(s-\mathrm{j}\omega_1)-\mathrm{j}K_{\mathrm{gd}}\right]G_{\mathrm{d}}(s-\mathrm{j}\omega_1)}{1-G_{\mathrm{d}}(s-\mathrm{j}\omega_1)+T_{\mathrm{PLL}}(s-\mathrm{j}\omega_1)\left\{G_{\mathrm{d}}(s-\mathrm{j}\omega_1)\left[H_{\mathrm{gi}}(s-\mathrm{j}\omega_1)-\mathrm{j}K_{\mathrm{gd}}\right]\boldsymbol{I}_{\mathrm{g1}}/2+\boldsymbol{U}_{\mathrm{g1}}/2\right\}} \tag{3}$$

$$Z_{\mathrm{gn}}(s)=\frac{R_{\mathrm{g}}+L_{\mathrm{g}}s-\left[H_{\mathrm{gi}}(s+\mathrm{j}\omega_1)+\mathrm{j}K_{\mathrm{gd}}\right]G_{\mathrm{d}}(s+\mathrm{j}\omega_1)}{1-G_{\mathrm{d}}(s+\mathrm{j}\omega_1)+T_{\mathrm{PLL}}(s+\mathrm{j}\omega_1)\left\{G_{\mathrm{d}}(s+\mathrm{j}\omega_1)\left[H_{\mathrm{gi}}(s+\mathrm{j}\omega_1)+\mathrm{j}K_{\mathrm{gd}}\right]\boldsymbol{I}^*_{\mathrm{g1}}/2+\boldsymbol{U}^*_{\mathrm{g1}}/2\right\}} \tag{4}$$

$$Z_{\mathrm{rp}}(s)=\frac{R_{\mathrm{s}}+R_{\mathrm{r}}^{'}/\sigma_{\mathrm{p}}(s)+(L_{\mathrm{ls}}+L_{\mathrm{lr}}^{'})s+H_{\mathrm{ri}}(s-\mathrm{j}\omega_1)G_{\mathrm{d}}(s-\mathrm{j}\omega_1)/\sigma_{\mathrm{p}}(s)}{1-T_{\mathrm{PLL}}(s-\mathrm{j}\omega_1)\left[\boldsymbol{I}_{\mathrm{r1}}H_{\mathrm{ri}}(s-\mathrm{j}\omega_1)G_{\mathrm{d}}(s-\mathrm{j}\omega_1)/\sigma_{\mathrm{p}}(s)-\boldsymbol{U}_{\mathrm{r1}}\right]/2} \tag{5}$$

$$Z_{\mathrm{rn}}(s)=\frac{R_{\mathrm{s}}+R_{\mathrm{r}}^{'}/\sigma_{\mathrm{n}}(s)+(L_{\mathrm{ls}}+L_{\mathrm{lr}}^{'})s+H_{\mathrm{ri}}(s+\mathrm{j}\omega_1)G_{\mathrm{d}}(s+\mathrm{j}\omega_1)/\sigma_{\mathrm{n}}(s)}{1-T_{\mathrm{PLL}}(s+\mathrm{j}\omega_1)\left[\boldsymbol{I}^*_{\mathrm{r1}}H_{\mathrm{ri}}(s+\mathrm{j}\omega_1)G_{\mathrm{d}}(s+\mathrm{j}\omega_1)/\sigma_{\mathrm{n}}(s)-\boldsymbol{U}^*_{\mathrm{r1}}\right]/2} \tag{6}$$

Typical double-loop PI controller are applied under synchronous reference frame (SRF). Phase-locked loop is used to synchronize WT terminal voltage with grid voltage. Neglecting the slow outer loop control dynamics, DC side dynamic and sequence-domain impedance coupling, the positive and negative sequence impedances of GSC and RSC branches are derived applying harmonic linearization [11], as represented by (3) – (6), where

$$H_{\mathrm{gi}}(s)=K_{\mathrm{gp}}+K_{\mathrm{gi}}/s,\ H_{\mathrm{ri}}(s)=K_{\mathrm{rp}}+K_{\mathrm{ri}}/s,$$

$$\sigma_{\mathrm{p}}(s)=\left(s-\mathrm{j}\omega_{\mathrm{r}}\right)/s,\ \sigma_{\mathrm{n}}(s)=\left(s+\mathrm{j}\omega_{\mathrm{r}}\right)/s,$$

$$H_{\mathrm{PLL}}(s)=\frac{K_{\mathrm{ppll}}+K_{\mathrm{ipll}}/s}{s},T_{\mathrm{PLL}}(s)=\frac{H_{\mathrm{PLL}}(s)}{1+\boldsymbol{U}_{\mathrm{g1}}H_{\mathrm{PLL}}(s)}$$

$\boldsymbol{I}_{\mathrm{g1}}$, $\boldsymbol{U}_{\mathrm{g1}}$ are the fundamental components of GSC terminal current and voltage, and $\boldsymbol{I}_{\mathrm{r1}}$, $\boldsymbol{U}_{\mathrm{r1}}$ are the fundamental components of RSC terminal current and voltage. Complete impedances of the simulated WT, i.e. Z_{WT} in both positive-and negative-sequence as illustrated in Fig. 2, can be obtained by solving parallel circuit impedance.

For HVDC connection, two-level VSC based converters are adopted here. Grid side VSC converter (GSVSC) controls the voltage of DC link, and constant DC voltage is assumed due to the connection with strong onshore grid. Wind farm side VSC converter (WFVSC) is regulated with a single-loop PI controller to maintain constant AC voltage for the connected wind farm [15], [20], [21]. A fixed clock signal is used to generate reference frequency for the regulated AC voltage. Applying harmonic linearization [22], the AC side sequence impedances of WFVSC as illustrated in Fig.2 can be derived as

$$Z_{\mathrm{VSC,p}}\left(s\right)=\frac{R_{\mathrm{c}}+sL_{\mathrm{c}}-\mathrm{j}K_{\mathrm{d}}K_{\mathrm{pwm}}G_{\mathrm{d}}\left(s-\mathrm{j}\omega_1\right)}{1+K_{\mathrm{pwm}}H_{\mathrm{v}}\left(s-\mathrm{j}\omega_1\right)G_{\mathrm{d}}\left(s-\mathrm{j}\omega_1\right)} \tag{7}$$

$$Z_{\mathrm{VSC,n}}\left(s\right)=\frac{R_{\mathrm{c}}+sL_{\mathrm{c}}+\mathrm{j}K_{\mathrm{d}}K_{\mathrm{pwm}}G_{\mathrm{d}}\left(s+\mathrm{j}\omega_1\right)}{1+K_{\mathrm{pwm}}H_{\mathrm{v}}\left(s+\mathrm{j}\omega_1\right)G_{\mathrm{d}}\left(s+\mathrm{j}\omega_1\right)} \tag{8}$$

where $G_{\mathrm{d}}\left(s\right)=1/\left(1+1.5T_{\mathrm{s}}s\right)$, $H_{\mathrm{v}}\left(s\right)=K_{\mathrm{vp}}+K_{\mathrm{vi}}/s$ and K_{pwm} is the gain of the PWM unit.

The derived analytical impedances of single 5 MW DFIG-based WT and HVDC converter are validated through numerical simulations, as presented in Fig. 3. As observed, the analytical models of both grid components match their simulation impedance responses well. The adopted two-level WFVSC shows capacitive characteristic at sub-synchronous frequencies, and such observations can be found for MMC-based HVDC converter using the same control strategy [20], [21], only not for the whole sub-synchronous frequency area.

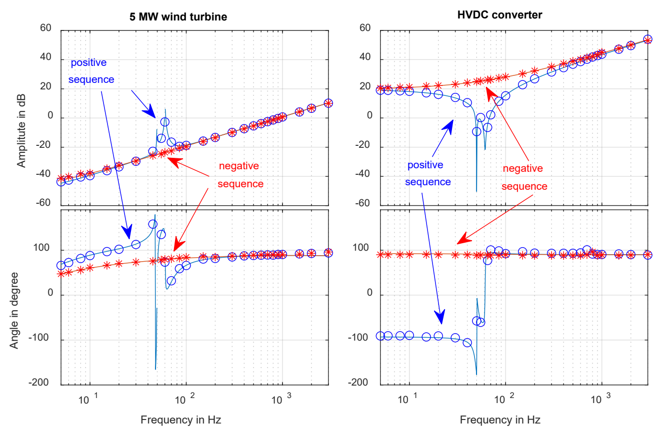

Fig. 3 Validation of sequence-domain impedance responses. Solid lines: analytical models; Asterisks and circles: numerical simulation results

As for passive grid components, all cables are represented by pi models, long-line correction is not needed due to the short length of each cable section. Transformers are modelled with short circuit impedances, and passive filter impedances are calculated according to their capacities and quality factors [20]. Additionally, the accuracy of the aggregated model of MV collector system is acceptable for resonance analysis, as validated in [5]. Note that all passive grid components have same positive- and negative sequence impedance models.

III. Resonance Analysis

Based on the sequence impedances of each grid component and the aggregation of MV collector system, the three-phase test grid in Fig. 2 can be analyzed with its single-line sequence-component circuits. Without losing generality, this paper focuses on the resonances in positive-sequence system. According to basic circuit theory, the 8-bus impedance network in Fig. 2 can be formulated into an 8-dimensional nodal admittance matrix $\boldsymbol{Y}_{\mathrm{NN}}(s)$ that relates the voltages and currents of the buses from B1 to B8, as represented by

$$\begin{bmatrix} I_{\mathrm{B1}} \\ I_{\mathrm{B2}} \\ \vdots \\ I_{\mathrm{B8}} \end{bmatrix}=\underbrace{\begin{bmatrix} Y_{11} & Y_{12} & \cdots & Y_{18} \\ Y_{21} & Y_{22} & \ddots & Y_{28} \\ \vdots & \ddots & \ddots & \vdots \\ Y_{81} & Y_{82} & \cdots & Y_{88} \end{bmatrix}}_{\boldsymbol{Y}_{\mathrm{NN}}(s)}\begin{bmatrix} U_{\mathrm{B1}} \\ U_{\mathrm{B2}} \\ \vdots \\ U_{\mathrm{B8}} \end{bmatrix} \tag{9}$$

Inversing and decomposing $\boldsymbol{Y}_{\mathrm{NN}}(s)$ according to matrix decoupling theory [17] yields the eigenvalue-based impedance matrix, also called modal impedance matrix

$$\boldsymbol{Z}_{\mathrm{M}}(s)=\boldsymbol{T}^{-1}\boldsymbol{Y}_{\mathrm{NN}}(s)^{-1}\boldsymbol{T}=\begin{bmatrix} Z_{\mathrm{m1}} & 0 & \dots & 0 \\ 0 & Z_{\mathrm{m2}} & \ddots & 0 \\ \vdots & \ddots & \ddots & \vdots \\ 0 & 0 & \dots & Z_{\mathrm{m8}} \end{bmatrix} \qquad (10)$$

where $\boldsymbol{T}$ is the right eigenvector matrix of $\boldsymbol{Y}_{\mathrm{NN}}(s)^{-1}$, Z_{m1}, Z_{m2} to Z_{m8} are system modal impedances. Fig. 4 shows the frequency scanning to the obtained modal impedances. The peaks in magnitude plot indicate resonances. When the damping of a resonance mode is negative, i.e. corresponding modal impedance with a negative real part, system stability is at risk. The negative damping is also indicated in the phase plot by a larger than 180° phase variation around resonance frequency. For modal impedance with positive damping, a larger peak value in amplitude plot means greater harmonic amplification effect at resonance frequency.

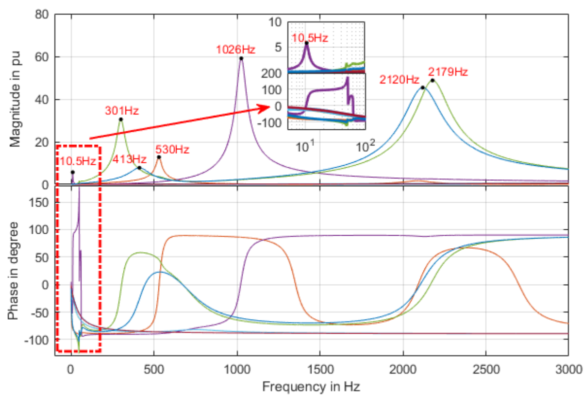

Fig. 4 Frequency scanning to the modal impedances of the test grid

After obtaining resonance frequencies and impedances, the most influential buses to each resonance mode could be determined through eigenvalue decomposition [17], [24]. The evaluation index is defined as participation factor (PF), as listed in Table III.

Modal Res.	f_{res} in Hz	10.5	301	413	530	1026	2120	2179
	$\lvert Z_{\mathrm{m}}\rvert$ in pu	5.7	31	7.8	12.8	59	45	49
***PF* in %**	B1	**25**	3	5	**14**	0	0	0
	B2	**15**	10	9	**16**	**31**	0	0
	B3	**15**	11	9	**15**	**31**	0	1
	B4	**15**	11	9	**15**	**31**	0	1
	B5	8	**16**	**17**	9	3	**27**	**26**
	B6	8	**16**	**17**	9	3	**27**	**26**
	B7	7	**17**	**18**	11	2	**23**	**23**
	B8	7	**17**	**18**	11	2	**23**	**23**

TABLE III. PARTICIPATION FACTORS OF DOMINATING RESONANCE MODES

For the 10.5 Hz resonance mode, the buses B1, B2, B3 and B4 in 155 kV high-voltage side contributes mostly to the formed LC resonance circuit, but as the source of negative damping at SSR frequencies [6], the buses B7 and B8 where DFIG-based WTs are located have larger impact on the risk of this SSR mode. For the 301 Hz, 413 Hz, 2120 Hz and the 2179 Hz resonance modes, the buses B5, B6, B7 and B8 in two MV collector systems have the largest PFs, thus are the main resonance sources. For the 530 Hz and 1026 Hz resonance modes, the buses B2, B3 and B4 where 155 kV AC cables are located play an important role, besides, the switching harmonic filters of HVDC converter in bus B1 also participate the 530 Hz resonance. Noted that the PFs in Table III are only valid for the operating condition when all WTs are in-service and generate full power.

A. *Impact of WT Rotor Speed*

WT usually works under the maximum power point tracking mode. The variation of wind speed to a lower value may cause WT output power decreases, and as follows, rotor speed will be decreased from its nominal value (1.2 pu). This behavior is included in the detailed DFIG model by following

$$\omega_{\mathrm{r}}^{*} = -0.67P^{2}+1.42P+0.51 \qquad (11)$$

as speed reference, where P denotes the feed-in active power from WT [25]. The speed reference ω_{r}^{*} slowly tracks changes in power P with a time constant of approximately 5 seconds.

Fig. 5 shows the impact of rotor speed on the modal impedances of the investigated system. Only SSR mode is displayed as the influence on other resonance modes is not observable. As rotor speed decreases, extra negative resistance will be introduced into WT at SSR frequencies. When the total resistance of the system becomes negative, SSR stability will be endangered. This is what happens under the conditions of rotor speed as 0.8 pu and 0.7 pu in Fig. 5. The larger than 180° phase variation around the SSR frequency indicates a negative part of the modal impedance at resonance frequency, i.e. negative damping.

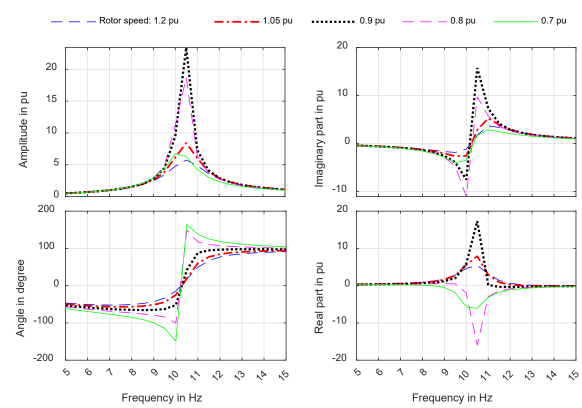

Fig. 5 Impact of rotor speed ω_{r} on system modal impedances

In order to validate this analytical result, simulation models are built up in MATLAB/Simulink, where the DFIG system is taken from the standard simulation model developed by MATLAB [25], only the change of parameters and minor modification of control structure are made. In time-domain simulation, wind speed is varied from 15 m/s to 5 m/s at t=6 s.

The variation of wind speed and outputs of the aggregated wind turbine WT1 are shown in Fig. 6. Diverging oscillation is observed when rotor speeds drops to be around 0.8 pu.

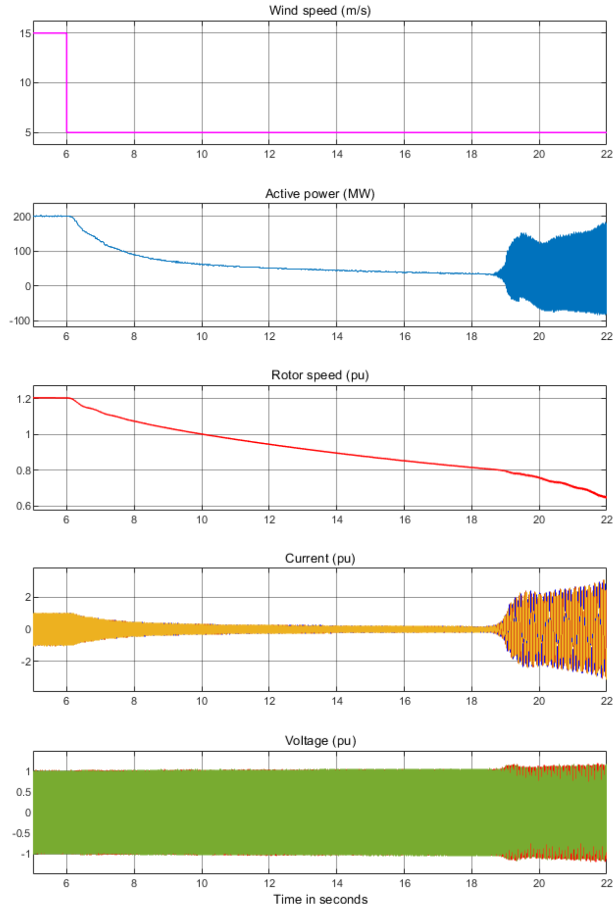

Fig. 6 Time-domain simulation outputs of the aggregated wind turbine WT1

Furtherly, FFT analysis is conducted to the voltage of the 155 kV AC bus B2, which interconnects OWF and HVDC. The results are shown in Fig. 7. Large SSR frequency component is observed at the starting stage of the diverging oscillation, and the mirror frequency component around 90 Hz is seen in the frequency spectrum.

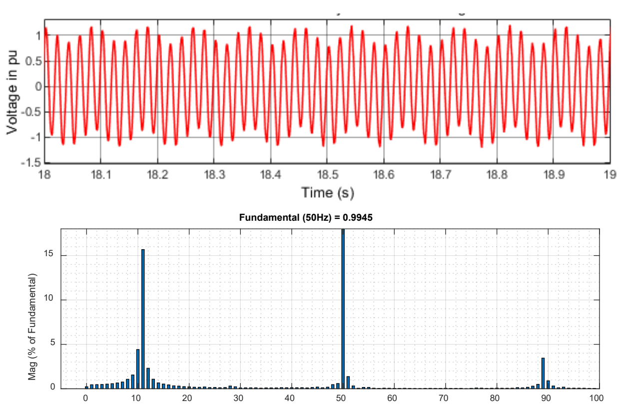

Fig. 7 FFT analysis to the voltage of 155 kV AC bus B2

Apart from the variation of wind speed, wind turbine output power could also be changed when wind farm receives a lowering power generation command from its superior level control center, then as a consequence, rotor speed might be regulated down and risk SSR stability.

B. Impact of the Variation of In-service Wind Turbines

In real life wind farm, individual WTs can be disconnected from grid by switching off their terminal breakers, or arrays of WTs can be disconnected from grid at the 33 kV AC bus, as shown in Fig. 8. Their impact on resonances will be addressed in this section separately.

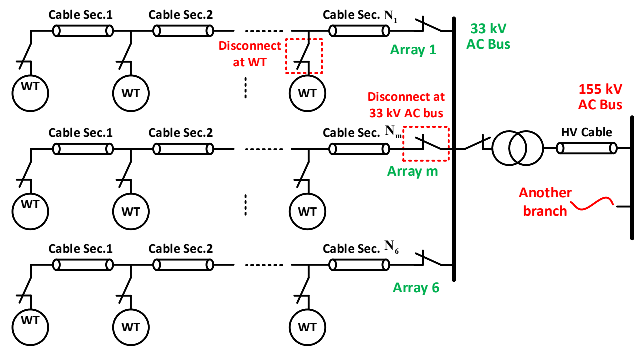

Fig. 8 Schematic diagram of WT disconnection at different locations

1) Disconnection of wind turbines at 33 kV AC bus

The change of wind array switching state can happen when wind farm is started or stopped, or when a lower generation control order is received from its superior level control center. The impact on resonance is shown in Fig. 9. At SSR frequencies, the phase variation around resonance frequency is far less than 180° for each scenario, so the impact on SSR stability is quite small. Besides, the amplitudes of modal impedances are no larger than 10 for all scenarios, thus the impact on amplification effect is neglectable. At frequencies above 200 Hz, negative damping has not been observed for each resonance mode, so only using the amplitude plot is sufficient for evaluating resonance amplification effect. The arrows in Fig. 9 b) indicate that as less wind arrays are connected into grids, the two resonance modes at above 2 kHz move from 2 kHz toward 3 kHz, the resonance mode at around 1 kHz moves from 1100 Hz toward 900 Hz, and the resonance mode at around 300 Hz moves from 300 Hz toward 400 Hz.

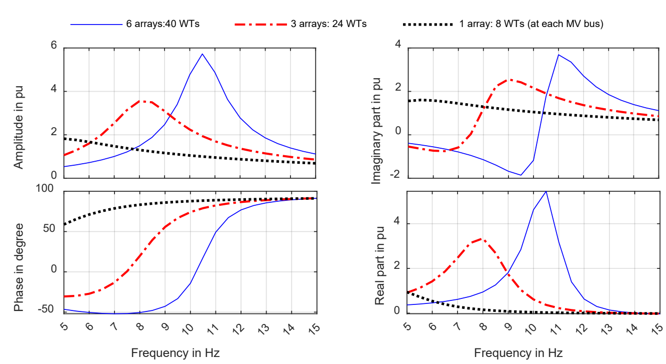

a) At SSR frequencies

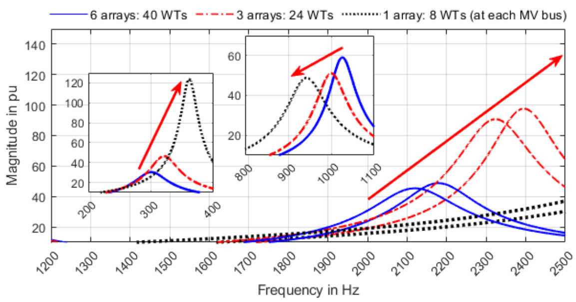

b) At frequencies above 200 Hz

Fig. 9 Frequency scanning of modal impedances when the number of connected wind arrays are varied

Stimulation of the resonance at around 350 Hz is validated by time-domain simulation. As shown in Fig. 10, after switching off 5 of the 6 wind arrays in each MV collector system at 4 s, the 350 Hz voltage component on 155 kV AC bus is greatly amplified. According to the recommended requirements on harmonic distortions in [1], the 350 Hz harmonic component violates the limit of 1.5% of fundamental value, and the total harmonic distortion (THD) of the 155 kV AC bus voltage violates the limit of 2.5% of fundamental value.

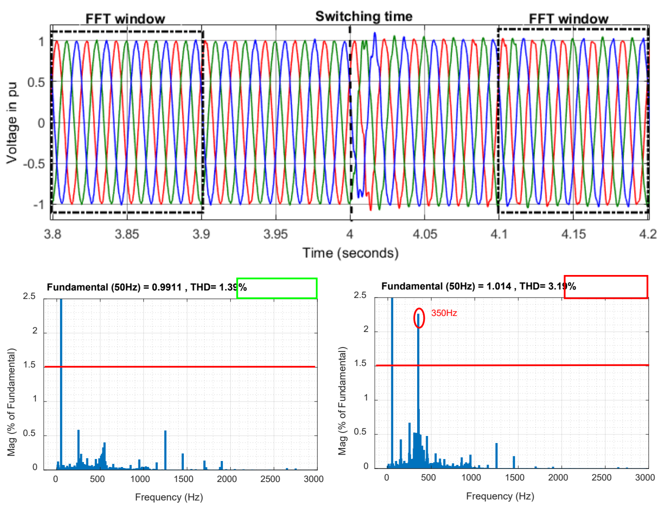

Fig. 10 Waveforms of the 155 kV AC bus voltage and FFT analysis

2) Disconnection of wind turbines at their terminals

Wind turbines can be disconnected from grids due to maintenance, fault or wind curtailment reasons. By quite low or high wind speed conditions, all WTs can be cut off from grids. The disconnection of WT can be operated through opening the high or low voltage side breakers of their 950 V / 33 kV step-up transformers or the breakers in RSC and GSC branches, as shown in Fig.11. Opening transformer low-voltage side breaker has almost the same effect as opening transformer high-voltage side breaker, as transformer shunt impedance of the excitation branch is far bigger than its series impedances in the primary and secondary windings, there is almost no current flowing into a transformer once one side is opened.

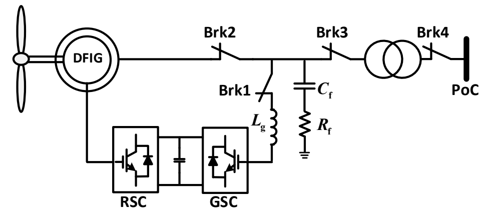

Fig. 11 Single line circuit of the simulated DFIG-based WT

Assuming that the disconnection of WTs does not influence the switching states of collector cables, then the impact of the number of connected WTs on modal impedances are shown in Fig. 12, both the situations of opening transformer breakers and opening GSC and RSC branch breakers are considered. Since their impact on the SSR resonance mode is very small, it is not displayed in the figure.

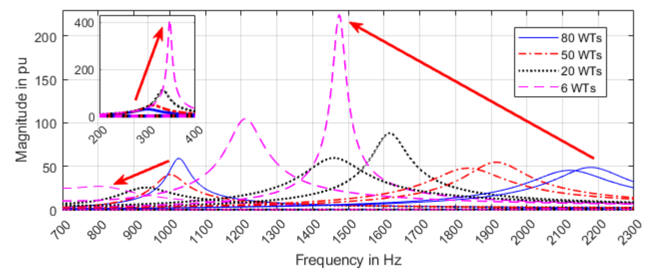

a) WT disconnected by opening transformer breaker

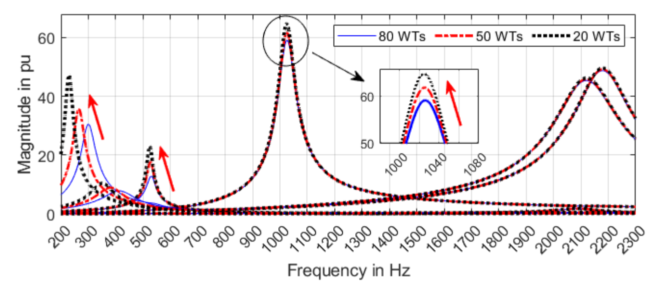

b) WT disconnected by opening GSC and RSC branch breakers

Fig. 12 Impact of the number of connected WTs on modal impedances

In case WT is disconnected from grid by opening one of the transformer breakers, the scenarios of 80, 50, 20 and 6 WTs staying connected in grid are shown in Fig.12 a). When only 6 WTs in the OWF staying connected, the resonance mode at around 300 Hz moves to be around 350 Hz and have a very sharp peak. The two resonance modes at above 2 kHz move toward 1 kHz as the number of grid-connected WTs reduces. When only 6 WTs is connected in grid, the large resonance peak between 1400 Hz and 1500 Hz falls in the area of the switching sideband frequency of HVDC converter (1450 Hz), thus amplification of switching harmonics from HVDC converter will happen. Stimulation of this resonance is observed in time-domain simulation, as shown in Fig.13. Both 350 Hz and 1450 Hz voltage components violate the requirements on distortion limits as specified in [1].

In case WT is disconnected from grid by opening GSC and RSC branch breakers, as shown in Fig.12 b), the number of in-service WTs has the greatest impact on the 301 Hz resonance mode, while the impact on other resonances modes, especially those at above 1 kHz, are negligible. As the number of grid-connected WTs decreases to be 50 or down to 20, the 301 Hz resonance will be moved to be around 250 Hz, and the typical 5th order harmonic can be slightly magnified. Since the overall amplification effect impact in this case is small, no simulation result will be presented.

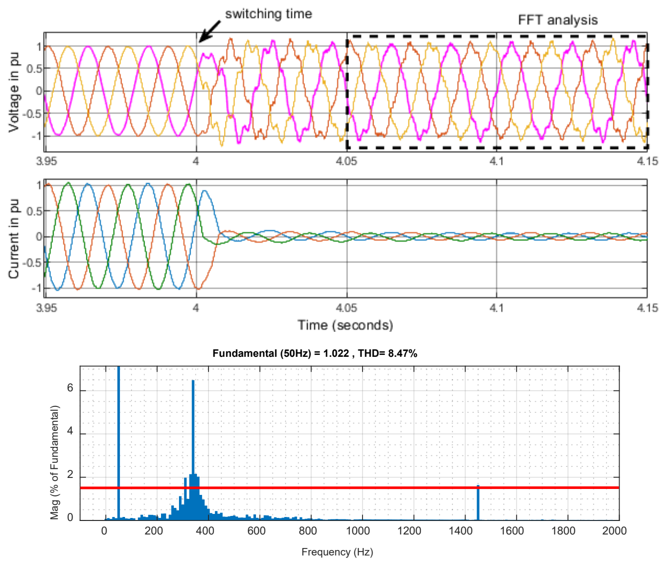

Fig.13 Voltage and current waveforms of the 155 kV AC bus B2 and FFT analysis

C. Discussion of Resonance Damping Strategies

If defining low frequency range as below 50 Hz, middle frequency range as between 50 Hz and 800 Hz, and high frequency range as above 800 Hz, then from the analysis of Section III. A and III. B, it is found resonances can occur at any frequency range. The resonance frequencies of low and middle frequency range does not vary much as wind farm operating condition changes, but the resonance frequencies of high frequency range may moves down to 1 kHz or up to 3 kHz or higher.

Low and middle frequency resonances could be damped by active controls of WT or HVDC converters [14], [26]. Since the switching frequencies of high power rating WT and HVDC converters are usually not greater than 2 kHz, their capability of controlling high frequency resonances are limited, so extra active damper with higher switching frequency could be used to address the high frequency resonance issue [27]. The resonance detection capability of the active damper in [27] makes it suitable for handling the enormous variation of resonance frequency resulted from operating condition change. Considering that the configuration of active control in DFIG converters for damping low and middle frequency resonances may involves dozens of WTs, it is less attractive than the damping configuration in HVDC converter. Therefore, the coordination of HVDC converter damping control and active damper may be a feasible solution for mitigating the resonances ranging from several Hz to a few kHz.

IV. Conclusion

This paper presented impedance-based resonance analysis for an exemplary DFIG-based offshore wind farm with HVDC connection. Derived impedance models of DFIG-based wind turbine and HVDC converter were validated through numerical simulations. The aggregated model of medium-voltage collector system is adjustable in reflecting the variation of in-service wind turbines and switching states of collector cables. The impact of different wind farm operating conditions on resonance frequency, amplification level and the occurrence of negative damping were analyzed applying the RMA method. SSR stability and harmonic distortion issues were demonstrated for the frequency range from 5 Hz to 3 kHz. Considering the involved wide frequency range of resonances, the coordination of HVDC converter active control and high-switching frequency active damper is suggested to be used in mitigating the found resonances.

References

[1] *IEEE Recommended Practice and Requirements for Harmonic Control in Electric Power Systems*, IEEE Std 519-2014 (Revision of IEEE Std 519-1992), vol., no., pp.1-29, 11 June 2014.

[2] C. Buchhagen, C. Rauscher, A. Menze, and J. Jung, “BorWin1 – first experiences with harmonic interactions in converter dominated grids,” in *Proceedings of International ETG Congress 2015*, 2015, pp. 1–7.

[3] C. Buchhagen, M. Greve, A. Menze, and J. Jung, “Harmonic stability - practical experience of a TSO,” in *Proceedings of the 15th Wind Integration Workshop*, 2016, pp. 1–6.

[4] M. Brendel and G. Traufetter, “Knall auf hoher See,” *Der Spiegel*, no. 35, pp. 71–72, Aug. 2014.

[5] Y. Zhang, C. Klabunde and M. Wolter, “Frequency-coupled Impedance Modelling and Resonance Analysis of DFIG-based Offshore Wind Farm with HVDC Connection,” *IEEE Access,* under review.

[6] X. Xie, X. Zhang, H. Liu, H. Liu, Y. Li and C. Zhang, “Characteristic Analysis of Subsynchronous Resonance in Practical Wind Farms Connected to Series-Compensated Transmissions,” in *IEEE Transactions on Energy Conversion*, vol. 32, no. 3, pp. 1117-1126, Sept. 2017.

[7] Y. Zhang, C. Klabunde and M. Wolter, “Harmonic Resonance Analysis for DFIG-based Offshore Wind Farm with VSC-HVDC Connection,” *2019 IEEE Milan PowerTech*, Milan, Italy, 2019, pp. 1-6.

[8] M. Quester, V. Yellisetti, F. Loku and R. Puffer, “Assessing the Impact of Offshore Wind Farm Grid Configuration on Harmonic Stability,” *2019 IEEE Milan PowerTech*, Milan, Italy, 2019, pp. 1-6.

[9] H. Jiang, J. You, H. Liu, W. Ning and L. Wu, “Impedance characteristics of DFIGs considering the impacts of DFIG numbers and locations and its application on SSR analysis,” *2017 IEEE Power & Energy Society General Meeting*, Chicago, IL, 2017, pp. 1-8.

[10] C. Zhang, X. Cai, M. Molinas and A. Rygg, “Frequency-domain modelling and stability analysis of a DFIG-based wind energy conversion system under non-compensated AC grids: impedance modelling effects and consequences on stability,” in *IET Power Electronics*, vol. 12, no. 4, pp. 907-914, 10 4 2019.

[11] I. Vieto and J. Sun, “Sequence Impedance Modeling and Analysis of Type-III Wind Turbines,” in *IEEE Transactions on Energy Conversion*, vol. 33, no. 2, pp. 537-545, June 2018.

[12] H. Zong, J. Lyu, X. Cai, C. Zhang, M. Molinas, F. Rao, “Accurate aggregated modelling of wind farm systems in modified sequence domain for stability analysis,” *Electric Power Systems Research*, Volume 175, 2019.

[13] L. Chen, H. Nian and Y. Xu, “Impedance Aggregation Method of Multiple Wind Turbines and Accuracy Analysis,” *Energies*, 2019, 12, 2035.

[14] M. Amin, and M. Molinas. “Understanding the Origin of Oscillatory Phenomena Observed Between Wind Farms and HVdc Systems,” *IEEE Journal of Emerging and Selected Topics in Power Electronics*, vol. 5, no. 1, pp.378–392, Mar. 2017.
[15] J. Lyu, X. Cai and M. Molinas, “Frequency Domain Stability Analysis of MMC-Based HVdc for Wind Farm Integration,” in *IEEE Journal of Emerging and Selected Topics in Power Electronics*, vol. 4, no. 1, pp. 141-151, March 2016.
[16] Z. Li, H. Hu, L. Tang, Y. Wang, T. Zang and Z. He, “Quantitative Severity Assessment and Sensitivity Analysis Under Uncertainty for Harmonic Resonance Amplification in Power Systems,” in *IEEE Transactions on Power Delivery*.
[17] Wilsun Xu, Zhenyu Huang, Yu Cui and Haizhen Wang, “Harmonic resonance mode analysis,” in *IEEE Transactions on Power Delivery*, vol. 20, no. 2, pp. 1182-1190, April 2005.
[18] ABB, “XLPE Submarine Cable Systems, Attachment to XLPE Land Cable Systems - User's Guide,” volume Rev 5, 2007.
[19] E. Muljadi et al., “Equivalencing the collector system of a large wind power plant,” *2006 IEEE Power Engineering Society General Meeting*, Montreal, Que., 2006, pp. 9 pp.-.
[20] J. Lyu, X. Cai, M. Amin and M. Molinas, “Sub-synchronous oscillation mechanism and its suppression in MMC-based HVDC connected wind farms,” in IET Generation, Transmission & Distribution, vol. 12, no. 4, pp. 1021-1029, 27 2 2018.
[21] J. Lyu, X. Cai and M. Molinas, “Optimal Design of Controller Parameters for Improving the Stability of MMC-HVDC for Wind Farm Integration,” in IEEE Journal of Emerging and Selected Topics in Power Electronics, vol. 6, no. 1, pp. 40-53, March 2018.
[22] M. Cespedes and J. Sun, “Impedance modeling and analysis of grid connected voltage-source converters,” *IEEE Trans. Power Electron.*, vol. 29, no. 3, pp. 1254–1261, Mar. 2014.
[23] W. Xu, “Component Modeling Issues for Power Quality Assessment, ” in *IEEE Power Engineering Review*, vol. 21, no. 11, pp. 12-17, Nov. 2001.
[24] C. Amornvipas, “Harmonic Studies and Resonance Analyses in Electrical Power Systems,” Ph.D. dissertation, Institute of Electric Power Systems, Eng., Univ. Hannover, Shaker Verlag, 2009.
[25] N. W. Miller, J. J. Sanchez-Gasca, W. W. Price and R. W. Delmerico, “Dynamic modeling of GE 1.5 and 3.6 MW wind turbine-generators for stability simulations,” *2003 IEEE Power Engineering Society General Meeting* (IEEE Cat. No.03CH37491), Toronto, Ont., 2003, pp. 1977-1983 Vol. 3.
[26] I. Vieto and J. Sun, “Damping of subsynchronous resonance involving Type-III wind turbines,” *2015 IEEE 16th Workshop on Control and Modeling for Power Electronics (COMPEL)*, Vancouver, BC, 2015, pp. 1-8.
[27] Y. Zhang, C. Klabunde, M. Wolter, “Harmonic Filtering in DFIG-based Offshore Wind Farm through Resonance Damping,” *IEEE ISGT Europe 2019*, Bucharest, 2019, pp. 1-5.